Supplementary Information: Tunable magnons in a dual-gated 2D antiferromagnet

Nele Stetzuhn[1,2], Abhijeet M. Kumar[1], Sviatoslav Kovalchuk[1], Denis Yagodkin[1], Louis Simon[1], Samuel Mañas-Valero[3,4], Eugenio Coronado[3], Takashi Taniguchi[6], Kenji Watanabe[6], Deepika Gill[2], Sangeeta Sharma[1,2], Piet Brouwer[1], Clemens von Korff Schmising[2,5], Stefan Eisebitt[2,5], Kirill I. Bolotin[1]

[1] Department of Physics, Freie Universität Berlin, Arnimallee 14, 14195 Berlin, Germany

[2] Max Born Institute for Nonlinar Optics and Short-Pulse Spectroscopy, Max-Born-Str. 2A, 12489 Berlin, Germany

[3] Instituto de Ciencia Molecular, Universidad de Valencia, Dr. Moliner 50, Burjasot, 46100, Spain

[4] Department of Quantum Nanoscience, Kavli Institute of Nanoscience, Delft University of Technology, Delft 2628CJ, the Netherlands

[5] Institut für Optik und Atomare Physik, Technische Universität Berlin, Straße des 17. Juni 135, 10623 Berlin, Germany

[6] National Institute for Materials Science, Namiki 1-1, Tsukuba, 305-0044, Ibaraki, Japan

1 Tr-reflectivity measurements

The single-color tr-reflectivity detection scheme is shown in Fig. 1a. To achieve a high signal-to-noise ratio in our experiments, we tune our pump and probe energies just below the X_B exciton resonance around 1.375 eV for low gate voltages (dark blue curve in Fig. 1b). For higher gate voltages, it becomes neccessary to tune pump and probe to the trion resonance at 1.35 eV, as the exciton fades (green curve in Fig. 1b). We see in Fig. 1c, that for intermediate gate voltages the signal at both resonances (orange: exciton, purple: trion) becomes weak, however, they allow us to observe oscillations at both resonances and we find the same frequency for f_{OP} (f_{IP} ambiguous at trion resonance). Additionally, we mount a permanent magnet in proximity to the sample to increase signal strength. To estimate the strength of the external magnetic field, we use the open source software FEMM4.2 [1] (Fig. 2). At the sample position, the field is around 100 mT. It should be noted that the exact position of the sample can differ slightly between the measurements of the three devices, resulting in differences of the external magnetic field. Also, the external field has in- and out-of-plane components, as evidenced by the observation of both f_{IP} and f_{OP} modes. We neglect this fact in the macrospin model.

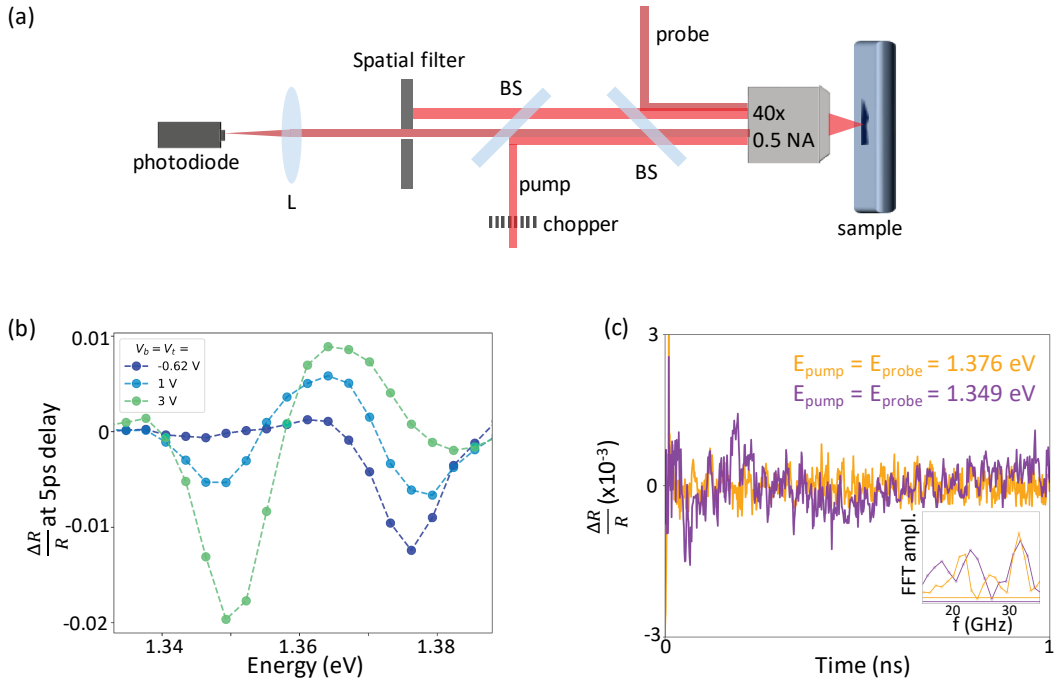

Figure 1: **Tr-reflecitivity measurement** (a) Detection scheme of single-color tr-reflectivity. (b) Tr-reflectivity spectra at small delay for different doping levels. The exciton resonance becomes weaker while the trion resonance strengthens for positive gate voltages. (c) Tr-reflectivity traces and extracted magnon frequencies (inset) measured at the exciton (orange) and trion (purple) resonances for $V_b = V_t = 3$ V after subtracting an exponential background.

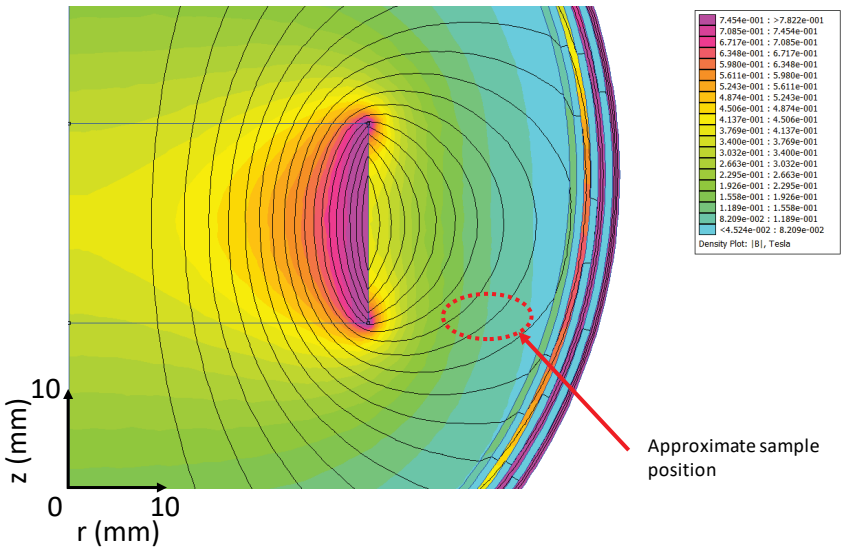

Figure 2: **Simulated field of permanent magnet used for experiments in the manuscript** Simulated magnetic field of the permanent magnet (Neodym 38, r = 3 mm) as a function of height z and radial distance r.

2 Temperature- and fluence-dependent magnon frequency shifts

To exclude laser- or gate-related heating effects as the origin of magnon frequency changes, fluence- and temperature dependent measurements were conducted on the trilayer sample. We see in Fig. 3a that a higher fluence leads to a downshift in magnon frequencies of $\Delta f_{\mathrm{IP}} \approx -(0.1 - 0.2\,\mathrm{GHz})$ and $\Delta f_{\mathrm{OP}} \approx -(0.4 - 0.8\,\mathrm{GHz})$. This consistent with absorption-induced heating of the sample, as the magnon frequencies also shift down with temperature (Fig. 3b). As shown in the main text, gating leads to an upshift of both magnon modes, so that we exclude heating as the underlying mechanism.

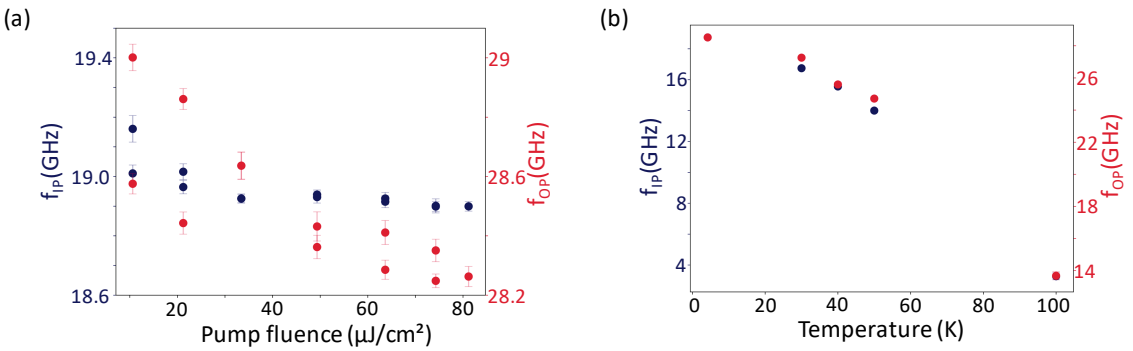

Figure 3: **Fluence- and temperature dependence of magnon modes** Shift of f_{IP} and f_{OP} as a function of (a) pump laser fluence and (b) sample temperature in the trilayer sample.

3 Gate-dependent PL and electrostatic modeling

To quantify the layer-resolved electron densities and electric fields, we follow the capacitor model suggested in [2, 3]. In this model, the CrSBr layers correspond to capacitor plates separated by a dielectric with $\epsilon_{\mathrm{CrSBr}}$ and spaced by interlayer distance $d_{\mathrm{CrSBr}} = 0.8\,\mathrm{nm}$. Using density functional theory (DFT), we calculate the out-of-plane $\epsilon_{\mathrm{CrSBr}}(E)$ for mono-, trilayer and bulk, shown in Fig. 4. As DC dielectric constants ($E = 0$), we find $\epsilon_{\mathrm{CrSBr}} = 3.8$ for a monolayer, $\epsilon_{\mathrm{CrSBr}} = 5.19$ for the trilayer and $\epsilon_{\mathrm{CrSBr}} = 7.42$ for the bulk. The graphite gates are modelled as capacitor plates with a dielectric of $\epsilon_{\mathrm{hBN}} = 3.76$ [4] and a thickness of the hBN flakes d_{hBN}. The equivalent circuit for the capacitor model for the trilayer is shown in Fig. 5a, and the resulting energy diagram in Fig. 5b. In the trilayer sample, the hBN thicknesses on both sides are $d_{\mathrm{hBN}} = 10\,\mathrm{nm}$.

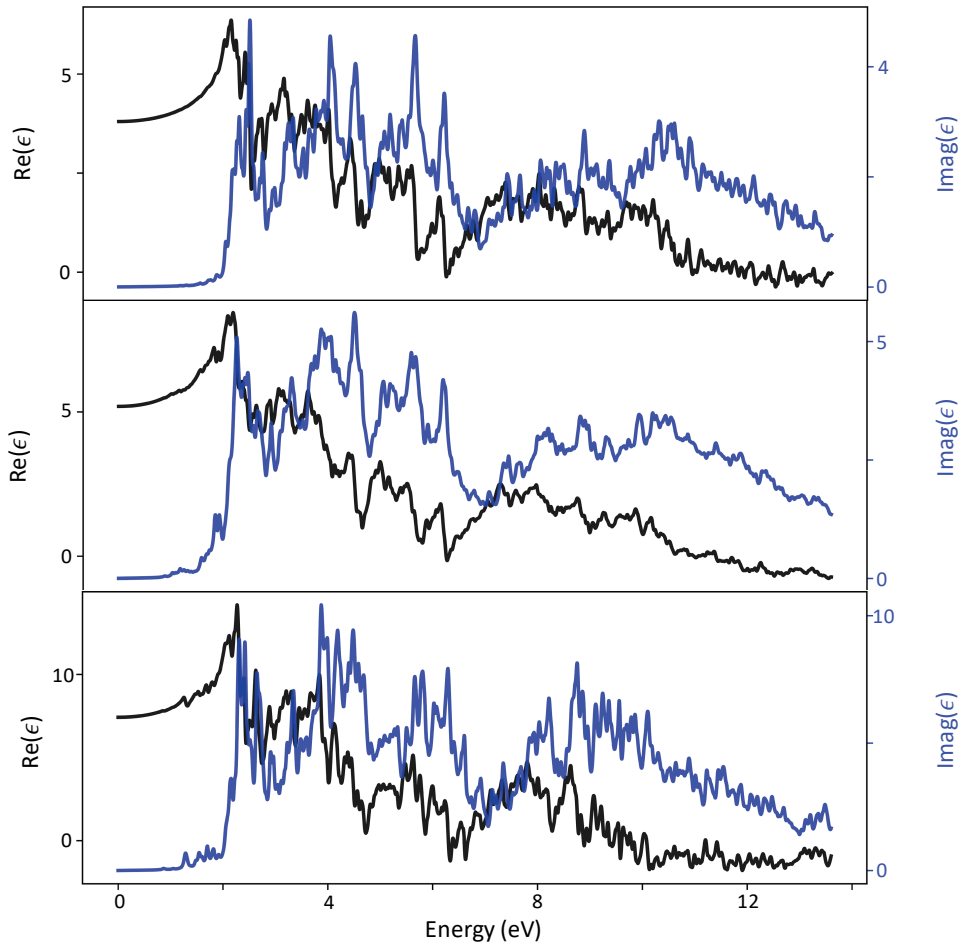

Figure 4: **Dielectric function of CrSBr** Calculated real and imaginary parts of the out-of-plane dielectric function of (a) monolayer, (b) trilayer and (c) bulk CrSBr.

The system of equations to extract the Fermi level with respect to the bottom of the conduction band $E_{F,i}$ (in eV, see

Fig. 5b) and the carrier density n_i (where i is top, middle and bottom) in the trilayer is as follows:

$$0 = (V_\mathrm{t} + V_{\mathrm{t},0}) - E_{\mathrm{F,t}} - \frac{en_\mathrm{t}}{C_\mathrm{t}} - \frac{C_\mathrm{CrSBr}}{C_\mathrm{t}}(E_{\mathrm{F,t}} - E_{\mathrm{F,m}}) \tag{1}$$

$$0 = (V_\mathrm{b} + V_{\mathrm{b},0}) - E_{\mathrm{F,b}} - \frac{en_\mathrm{b}}{C_\mathrm{t}} - \frac{C_\mathrm{CrSBr}}{C_\mathrm{b}}(E_{\mathrm{F,b}} - E_{\mathrm{F,m}}) \tag{2}$$

$$0 = -en_\mathrm{m} - \frac{C_\mathrm{CrSBr}}{e}(E_{\mathrm{F,m}} - E_{\mathrm{F,t}}) - \frac{C_\mathrm{CrSBr}}{e}(E_{\mathrm{F,m}} - E_{\mathrm{F,b}}). \tag{3}$$

Here $C_\mathrm{CrSBr} = \frac{\epsilon_0 \epsilon_\mathrm{CrSBr}}{d_\mathrm{CrSBr}}$ and $C_\mathrm{t/b} = \frac{\epsilon_0 \epsilon_\mathrm{hBN}}{d_{hBN,t/b}}$. To calculate the electron densities, we assume a two-dimensional density of states (DOS) similar to that in TMDs [3]. We note that behavior suggesting a one-dimensional DOS has been reported in CrSBr [5], which would lead to a stronger increase in n for energies just above the conduction band due to the emergence of van't Hove singularities. However, the overall dependence of n and F on the gate voltages, and therefore the main results of the manuscript, will not change with a different DOS.

In the PL data of the main manuscript we observe two key features which are of importance for the electrostatic modeling: Our CrSBr crystals are intrinsically n-doped (signified by the dominance of trions over excitons at zero gate voltage) and our samples have a built-in electric field (as shown by the field dependence of the middle layer exciton-to-trion ratio). To model the intrinsic n-doping, we introduce positive offset voltages $V_{\mathrm{t},0}$ and $V_{\mathrm{b},0}$ in Eq. (3) – corresponding to a downshift of the conduction bands of all layers with respect to the vacuum level. To model the built-in electric field, we use $V_{\mathrm{t},0} \neq V_{\mathrm{b},0}$ to introduce an offset between the conduction bands across layers.

To find reasonable values for $V_{\mathrm{t},0}$ and $V_{\mathrm{b},0}$, we use the exciton-to-trion ratios $I_\mathrm{B} = \frac{I_{X_\mathrm{B}}}{I_{X_\mathrm{B}^-}}$ and $I_{\mathrm{B}'} = \frac{I_{X'_\mathrm{B}}}{I_{X'^-_\mathrm{B}}}$ as indicators for the carrier densities of the outer layers, $n_\mathrm{t} + n_\mathrm{b}$, and the middle layer, n_m. As it is difficult to directly correlate I_B and $I_{\mathrm{B}'}$ to the electron densities by fitting (especially as we cannot 'resolve' n_t and n_b separately in the PL), we manually vary the offset voltages in the model to match the onset of doping to drops in the exciton-to-trion ratios.

From the symmetric behavior of I_B in Fig. 5c we deduce the following:

- We see the highest exciton-to-trion ratio I_B when both V_b and $V_\mathrm{t} < -0.8\,\mathrm{V}$. This means that increasing either gate voltage above this value should result in at least one of the layers being electron doped.
- When varying only one of the gate voltages while fixing the other to a sufficiently negative value, either the top or bottom layer stays almost undoped, as I_B stays nearly constant after an initial drop.
- When both V_b and $V_\mathrm{t} > 0\,\mathrm{V}$, both top and bottom layers should be electron-doped, as $I_\mathrm{B} \approx 0$ for those ranges of the gating diagram.

This gives us an upper limit for $V_{\mathrm{t},0}$ and $V_{\mathrm{b},0}$ of $\sim 2.5\,\mathrm{V}$, as increasing the offset voltages beyond this limit would mean that the sample is doped in the top or bottom layer for all gate voltages we reach in the experiment.

In the gate-dependence of $I_{\mathrm{B}'}$ in Fig. 5d, we see that

- $I_{\mathrm{B}'}$ drops faster when applying a top gate voltage. From this, we infer that $V_{\mathrm{t},0} < V_{\mathrm{b},0}$, because a smaller V_t is then sufficient to dope the middle layer.

We find that $V_{\mathrm{t},0} = 1\,\mathrm{V}$ and $V_{\mathrm{b},0} = 1.7\,\mathrm{V}$ fulfill all the requirements mentioned above and adequately reproduce the behavior seen in PL. The resulting layer-resolved doping maps are shown in Fig. 5e-g, with contour lines for selected doping levels ($0.5 - 3 \times 10^{12}\,\mathrm{cm}^{-2}$).

We show the same contour lines as guides to the eye in the experimental I_B and $I_{\mathrm{B}'}$ maps in Fig. 5c, d. In Fig. 5c, we see that the contour lines show the same symmetry with gates as I_B, and we see a drop in I_B for a similar n_t or n_b

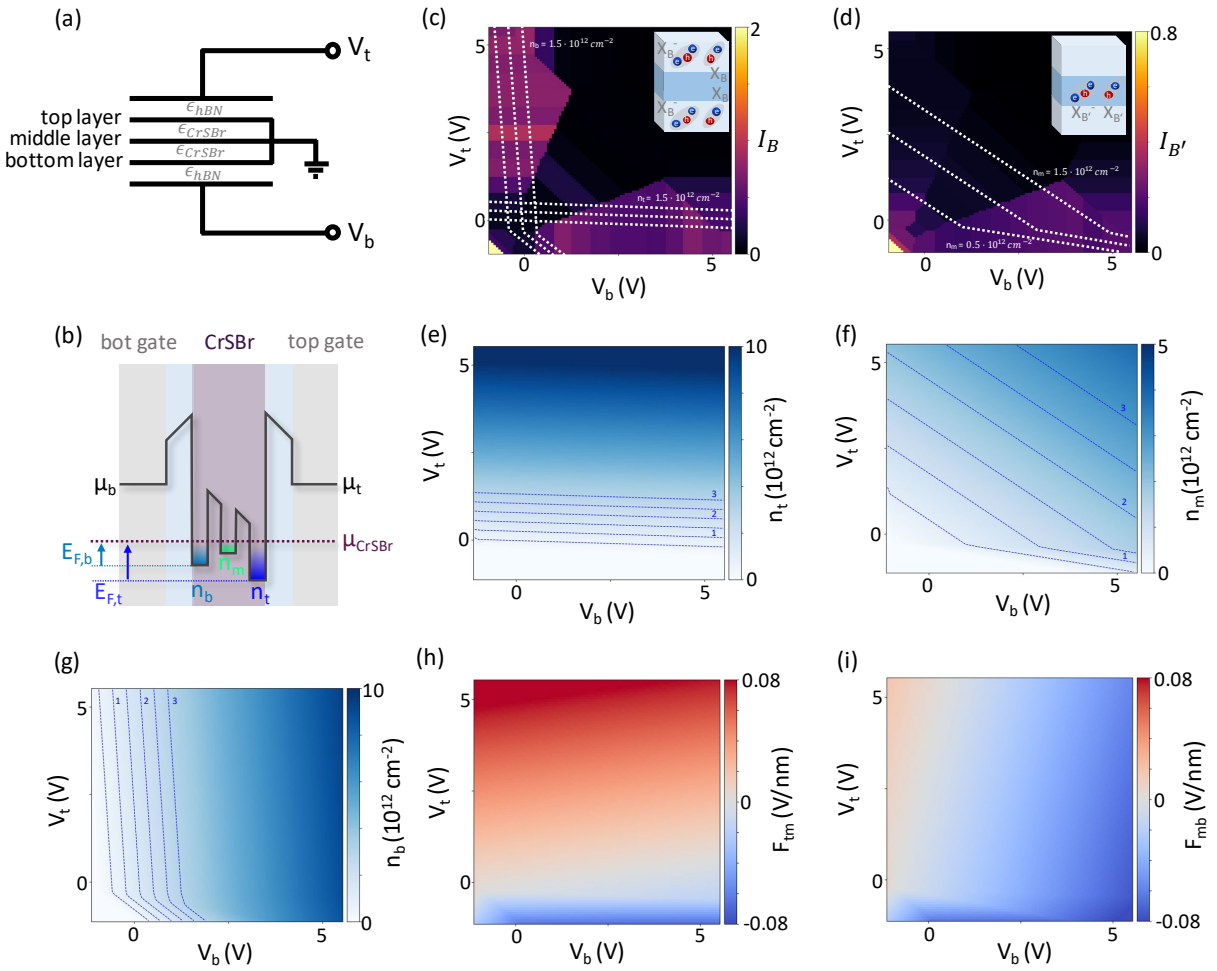

Figure 5: **Photoluminescence and electrostatic model of trilayer CrSBr** (a) Scheme of the capacitor model for a trilayer CrSBr with top and bottom gate and hBN dielectric. (b) Band alignment sketch when the sample is doped. The Fermi energies $E_{\mathrm{F},i}$ are defined as the difference between the conduction band and the chemical potential μ_{CrSBr}. The top and bottom gate voltages control μ_t and μ_b. (c) Exciton-to-trion ratio I_B for excitons and trions localized to top and bottom layer (see inset). The white dashed lines are guides to the eye corresponding to the contour lines for n_t and n_m being 0.5, 1 and $1.5 \times 10^{12}\,\mathrm{cm}^{-2}$ shown in (e), (g). (d) Exciton-to-trion ratio $I_{\mathrm{B}'}$ for excitons and trions localized in the middle layer (see inset). The white dashed lines are guides to the eye corresponding to the contour lines for $n_\mathrm{m} = 0.5$, 1 and $1.5 \times 10^{12}\,\mathrm{cm}^{-2}$ shown in (f). (e-g) Electron density in the top (e), middle (f) and bottom (g) layer. The contour lines show densities of 0.5, 1, 1.5, 2, 2.5 and $3 \times 10^{12}\,\mathrm{cm}^{-2}$. (h-i) Electric field between top and middle (h) and middle and bottom (i) layers.

(around $\sim 1.5 \times 10^{12}\,\mathrm{cm}^{-2}$). In Fig. 5d, the asymmetry of the contour line for $n_\mathrm{m} = 0.5 \times 10^{12}\,\mathrm{cm}^{-2}$ shows that we need a higher V_b to dope the middle layer when $V_\mathrm{t} < 0$ than in the opposite case. The modeled n_m also shows a quick increase when increasing V_t for large enough V_b, concurrent with a drop in $I_{\mathrm{B}'}$ in the same case. While the onset of the n_m happens for slightly lower gate voltages than the drop in $I_{\mathrm{B}'}$, the offset voltages of $V_{\mathrm{t},0} = 1\,\mathrm{V}$ and $V_{\mathrm{b},0} = 1.7\,\mathrm{V}$ give the best overall correlation between modeling and PL data. The gate-dependent electric fields between the layers are

shown in Fig. 5h, i.

It should be noted that changing the offset voltages slightly does not change the overall predicted behavior of the frequencies in the macrospin model (i.e. the gate sensitivity or frequency range). It can, however, slightly change the onset of frequency shifts as well as the fitted ν_a, ν_E and η_γ.

3.1 Gate-dependent PL and electrostatic model of 5-layer device

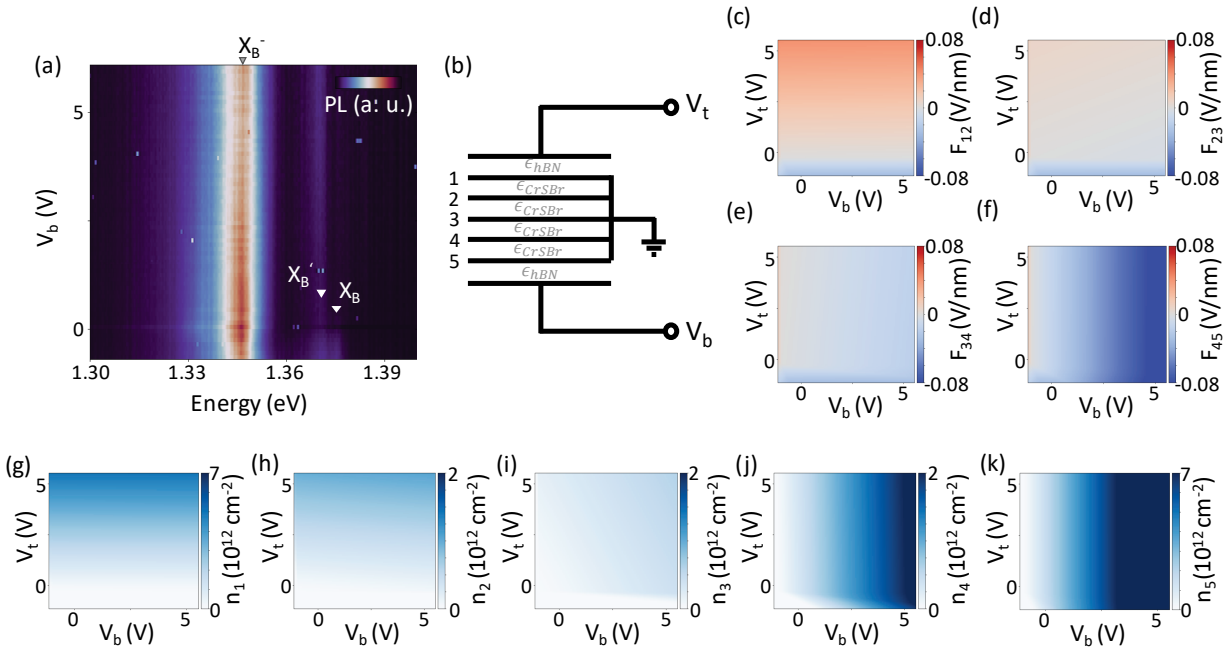

Figure 6: **Photoluminescence and electrostatic model of 5-layer CrSBr** (a) V_b-dependent photoluminescence map of the 5-layer CrSBr device. (b) Scheme of the capacitor model for a 5-layer CrSBr with top and bottom gate and hBN dielectric. (c-f) Electric field between the respective layers (numbering see (b)). (g-k) Electron density in the respective layers (numbering see (b)).

The gate-dependent photoluminescence of the 5-layer device in Fig. 6a again shows two split excitonic peaks at $X_B \approx 1.376\,\text{eV}$ and $X_B' \approx 1.370\,\text{eV}$, which we hypothesize to reside in the outer and inner layers, respectively. The intensities of the excitonic peaks for the undoped sample ($V_b < 0\,\text{V}$) are now comparable, which we attribute to the increased number of layers hosting X_B' excitons. In this device we could only apply a bottom gate voltage. For $V_b > 0\,\text{V}$, the intensity of the X_B exciton drops, and the trion resonance around 1.345 eV brightens. Meanwhile, the X_B' exciton remains visible for all measured gate voltages.

When modeling the 5-layer device as shown in Fig. 6b, we expand the system of equations to

$$0 = (V_t + V_{t,0}) - E_{F,1} - \frac{en_1}{C_t} - \frac{C_{CrSBr}}{C_t}(E_{F,1} - E_{F,2}) \tag{4}$$

$$0 = (V_b + V_{b,0}) - E_{F,5} - \frac{en_5}{C_b} - \frac{C_{CrSBr}}{C_b}(E_{F,5} - E_{F,4}) \tag{5}$$

$$0 = -en_2 - \frac{C_{CrSBr}}{e}(E_{F,2} - E_{F,1}) - \frac{C_{CrSBr}}{e}(E_{F,2} - E_{F,3}) \tag{6}$$

$$0 = -en_3 - \frac{C_{CrSBr}}{e}(E_{F,3} - E_{F,2}) - \frac{C_{CrSBr}}{e}(E_{F,3} - E_{F,4}) \tag{7}$$

$$0 = -en_4 - \frac{C_{CrSBr}}{e}(E_{F,4} - E_{F,3}) - \frac{C_{CrSBr}}{e}(E_{F,4} - E_{F,5}) \tag{8}$$

The hBN thicknesses in the 5-layer device are $d_{hBN,top} = 5\,\text{nm}$ and $d_{hBN,bot} = 10.5\,\text{nm}$. We use the trilayer

$\epsilon_{\mathrm{CrSBr}} = 5.19$ calculated with DFT (Fig. 4b). We assume the same offset voltages $V_{\mathrm{t},0}$ and $V_{\mathrm{b},0}$ as for the trilayer device. This leads to n_4 and n_5 increasing around $V_{\mathrm{b}} \approx -0.5\,\mathrm{V}$, in good agreement with the drop in $I_{\mathrm{B}'}$ shortly after. We also see that the charge carrier densities in the center layer remain below $\approx 1 \times 10^{12}\,\mathrm{cm}^{-2}$ for all applied gate voltages (Fig. 6i), which agrees with the visibility of X'_{B} for all gate voltages. All the calculated fields and electron densities for the 5-layer device are shown in Fig. 6c-k.

3.2 Gate-dependent PL and electrostatic model of 8-layer device

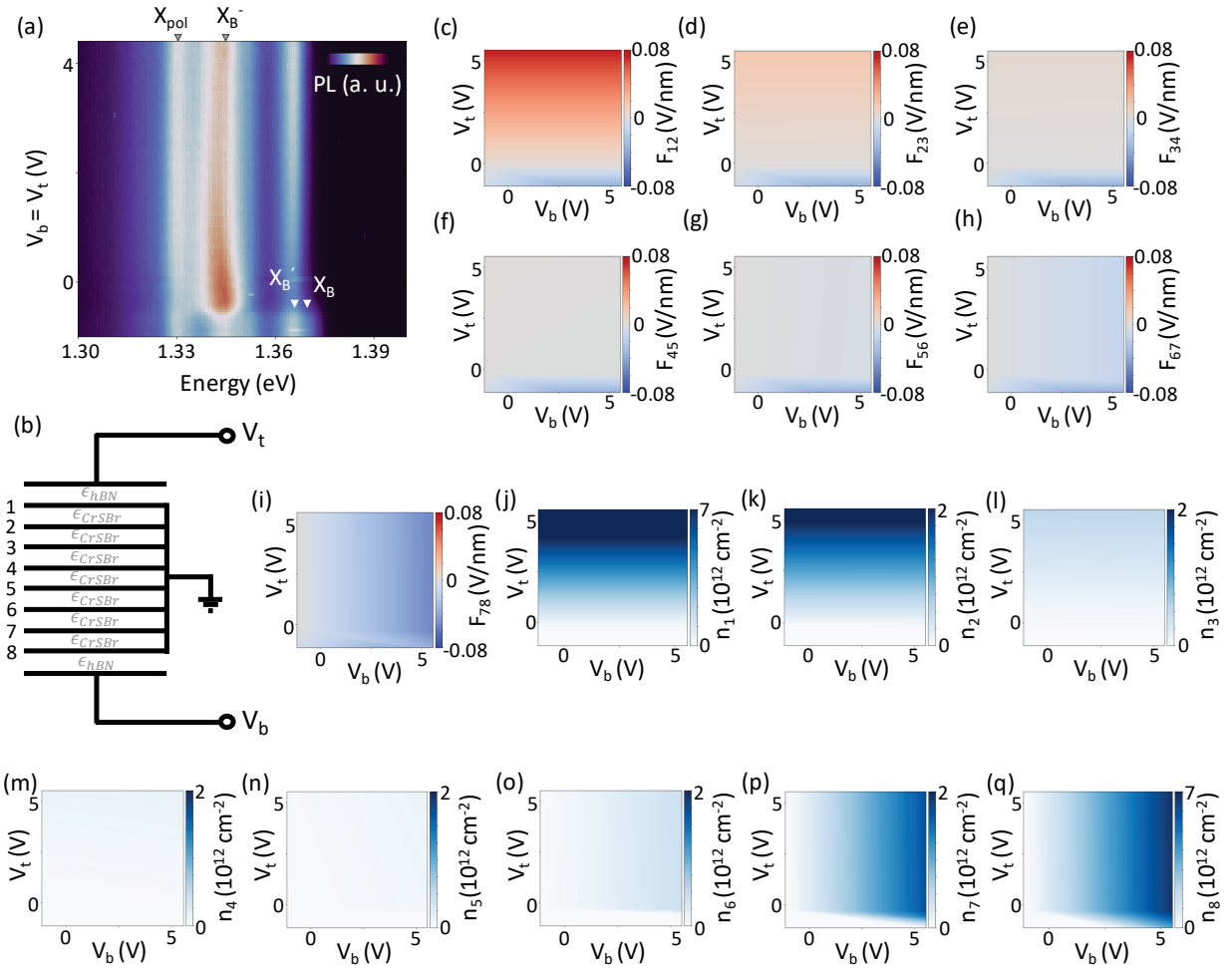

Figure 7: **Photoluminescence and electrostatic model of 8-layer CrSBr** (a) Gate-dependent photoluminescence map of the 8-layer CrSBr device. (b) Scheme of the capacitor model for an 8-layer CrSBr with top and bottom gate and hBN dielectric. (c-h) Electric field between the respective layers (numbering see (b)). (i-q) Electron density in the respective layers (numbering see (b)).

In the doping-dependent photoluminescence of the 8-layer device in Fig. 7a, we once again see two split excitonic peaks at $X_{\mathrm{B}} \approx 1.372\,\mathrm{eV}$ and $X'_{\mathrm{B}} \approx 1.366\,\mathrm{eV}$. In contrast to the tri- and 5-layer device, the X'_{B} peak is more intense than X_{B}, the latter only visible as a high-energy shoulder. This is consistent with X'_{B} emission stemming from excitons localized to the inner layers, as the number of such inner layers has increased from the 3- to 8-layer device.
We see X_{B} disappear for $V_{\mathrm{b}} = V_{\mathrm{t}} > -0.3\,\mathrm{V}$, simultaneously with a brightening of the trion resonance around 1.345 eV.

The X'_B exciton remains visible for all measured gate voltages, similarly to the 5-layer device. Additional peaks X_{pol} are visible in the 8-layer device PL at lower energies, possibly stemming from polaritons due to the increased sample thickness [6].

We expand the electrostatic model to 8 layers (Fig. 7b) in the same manner as for 5 layers. We measure the hBN thicknesses to be $d_{hBN,top} = 10\,\text{nm}$ and $d_{hBN,bot} = 6\,\text{nm}$ with AFM. Due to the increased thickness of the device, we use the bulk dielectric constant $\epsilon_{\text{CrSBr}} = 7.42$ calculated with DFT (Fig. 4c). We again assume the same offset voltages $V_{t,0}$ and $V_{b,0}$ used for the other devices. The resulting increase of electron density in the bottom layer n_8 around $V_b = V_t \approx -0.4\,\text{V}$ (Fig. 7q), followed by the top layer n_1 around $V_b = V_t \approx -0.2\,\text{V}$ correlates well with the drop in the exciton intensity we observe at $V_b = V_t > -0.3\,\text{V}$. The middle layers of the 8-layer device remain almost undoped (Fig. 7m, n). All the calculated fields and electron densities for the 8-layer device are shown in Fig. 7c-q.

4 Bulk macrospin model

For bulk antiferromagnets, we assume two coupled macrospins which repeat itself in periodic boundary conditions. We can write the LL equation

$$\frac{d\vec{m}_{1,2}}{dt} = -\gamma \vec{m}_{1,2} \times \vec{H}_{\text{eff}_{1,2}} \tag{9}$$

where $\vec{m}_{1,2}$ are the macrospins in neighboring layers. The effective field $\vec{H}_{\text{eff}_{1,2}}$ can be obtained from the energy E of the system:

$$E = H_0 \hat{c} \cdot (\vec{m}_1 + \vec{m}_2) - H_E \vec{m}_1 \cdot \vec{m}_2 + \frac{1}{2} H_a ((m_1^a)^2 + (m_2^a)^2) + \frac{1}{2} H_b ((m_1^b)^2 + (m_2^b)^2) \tag{10}$$

$$\vec{H}_{\text{eff}_{1,2}} = -\nabla_{\vec{m}_{1,2}} E = H_0 \hat{c} - H_E \vec{m}_{2,1} + H_a m_{1,2}^a \hat{a} + H_b m_{1,2}^b \hat{b}. \tag{11}$$

Here, $\hat{a}, \hat{b}, \hat{c}$ point along the corresponding crystallographic axes of CrSBr. H_b describes the easy axis magnetic anisotropy and H_a the intermediate one. H_E is the interlayer exchange interaction, which aligns the neighboring macrospins antiparallely. The external magnetic field $\vec{H}_0 = H_0 \hat{c}$ is assumed out-of-plane and determines the initial tilt θ of the macrospins away from the easy $\hat{b}$-axis.

As H_0 does not saturate the spins along the $\hat{c}$-axis, the equilibrium macrospins can be written as $\vec{m}_{1,2_0} = (0, \sin\theta, \pm\cos\theta)$. By inserting this expression into Eq. (21), we find θ by minimizing the equilibrium energy, $\frac{dE}{d\theta} = 0$, leading to the condition

$$H_0 = \sin\theta (H_b + 2H_E). \tag{12}$$

Next, we express the macrospins as $\vec{m}_{1,2} = \vec{m}_{1,2_0} + \delta\vec{m}_{1,2}$, where $\delta\vec{m}_{1,2} << \vec{m}_{1,2_0}$ are small deviations from equilibrium after excitation. By linearizing the LL equation, we arrive at

$$\frac{d}{dt}\delta\vec{m}_{1,2} = -\gamma \left(\delta\vec{m}_{1,2} \times \vec{H}^0_{\text{eff}_{1,2}} + \vec{m}_{1,2_0} \times \delta\vec{H}_{eff_{1,2}} \right) \tag{13}$$

where $\vec{H}_{\text{eff}_{1,2}} = \vec{H}^0_{\text{eff}_{1,2}} + \delta\vec{H}_{\text{eff}_{1,2}}$.

From the condition $\vec{m}_{1,2_0} \cdot \delta\vec{m}_{1,2} = 0$, we obtain $\delta\vec{m}_{1,2} = \left(\delta m^a_{1,2}, \mp\delta m^{||}_{1,2} \cos\theta, \delta m^{||}_{1,2} \sin\theta\right)$. Inserting this into Eq. (13) and using the ansatz $\delta\vec{m}_{1,2}(t) = \delta\vec{m}_{1,2}(t=0)e^{-i\omega t}$ results in

$$\frac{i\omega}{\gamma} \begin{pmatrix} \delta m_1^a \\ \delta m_1^{||} \\ \delta m_2^a \\ \delta m_2^{||} \end{pmatrix} = \begin{pmatrix} 0 & -H_E - H_b \cos^2\theta & 0 & H_E \cos(2\theta) \\ H_E + H_b - H_a & 0 & H_E & 0 \\ 0 & H_E \cos(2\theta) & 0 & -H_E - H_b \cos^2\theta \\ H_E & 0 & H_E + H_b - H_a & 0 \end{pmatrix} \begin{pmatrix} \delta m_1^a \\ \delta m_1^{||} \\ \delta m_2^a \\ \delta m_2^{||} \end{pmatrix}. \tag{14}$$

Solving this equation gives an analytical solution for the eigenvalues:

$$\begin{aligned} f_{\mathrm{IP}} &= \pm\frac{\gamma}{2\pi}\sqrt{(H_\mathrm{b}-H_\mathrm{a})(H_\mathrm{b}+2H_\mathrm{E})\left(1-\frac{H_0^2}{(2H_\mathrm{E}+H_\mathrm{b}-H_\mathrm{a})^2}\right)} \\ f_{\mathrm{OP}} &= \pm\frac{\gamma}{2\pi}\sqrt{(H_\mathrm{b}-H_\mathrm{a}+2H_\mathrm{E})(H_\mathrm{b}+2H_\mathrm{E})\left(2H_\mathrm{E}\frac{H_0^2}{(2H_\mathrm{E}+H_\mathrm{b}-H_\mathrm{a})^2}-H_\mathrm{b}\left(\frac{H_0^2}{(2H_\mathrm{E}+H_\mathrm{b}-H_\mathrm{a})^2}-1\right)\right)}. \end{aligned} \tag{15}$$

As the ansatz assumes that every second macrospin is exactly the same, these two solutions correspond to the case of zero momentum magnons (i.e. f_{IP} and f_{OP} in bulk experiments).

For magnons with $k_z \neq 0$, however, there is a phase difference between every second macrospin. Including this into the solutions of Eq. (13) gives an analytical solution for the dispersion along k_z. The phase difference changes the interlayer exchange term in the effective field of each macrospin $\vec{m}_i$ (where i is the layer number), since the macrospins above and below are no longer exactly the same. The effective field in layer i becomes

$$\vec{H}_{\mathrm{eff}_i} = H_0\hat{c} - \frac{1}{2}H_\mathrm{E}(\vec{m}_{i-1}+\vec{m}_{i+1}) + H_\mathrm{a}m_i^a\hat{a} + H_\mathrm{b}m_i^b\hat{b}. \tag{16}$$

To solve the new LL equation, we assume the following: Before the excitation, the equilibrium macrospins in every second layer are the same, $\vec{m}_{i+1_0} = \vec{m}_{i-1_0}$. For the deviations after the excitations, we use a plane wave ansatz $\delta\vec{m}_j(t) = \delta\vec{m}_j(t=0)e^{-i\omega t}e^{ik_z j d_z}$, where d_z is the interlayer spacing in z-direction and j describes the layer number. Inserting the new exchange term from Eq. (16) in Eq. (13) gives rise to the terms

$$\sim H_\mathrm{E}\begin{pmatrix}\delta m_i^{||}(\cos^2\theta-\sin^2\theta)\\ \delta m_i^a\cos\theta\\ \delta m_i^\mathrm{a}\sin\theta\end{pmatrix} - H_\mathrm{E}\begin{pmatrix}\delta m_{i-1}^{||}(\sin^2\theta-\cos^2\theta)\\ \delta m_{i-1}^a\cos\theta\\ -\delta m_{i-1}^a\sin\theta\end{pmatrix}(1+e^{-2ik_z d_z}) \tag{17}$$

which are the same as the ones found for $k_z = 0$, apart from the last term $\propto e^{-2ik_z d_z}$. This changes the matrix equation from Eq. (14) to:

$$\frac{i\omega}{\gamma}\begin{pmatrix}\delta m_1^a\\ \delta m_1^{||}\\ \delta m_2^a\\ \delta m_2^{||}\end{pmatrix} = \begin{pmatrix}0 & -H_\mathrm{E}-H_\mathrm{b}\cos^2\theta & 0 & H_\mathrm{E}\cos(2\theta)\left(1+e^{-2ik_z\cdot d_z}\right)\\ H_\mathrm{E}+H_\mathrm{b}-H_\mathrm{a} & 0 & H_\mathrm{E}\left(1+e^{-2ik_z\cdot d_z}\right) & 0\\ 0 & H_\mathrm{E}\cos(2\theta)\left(1+e^{-2ik_z\cdot d_z}\right) & 0 & -H_\mathrm{E}-H_\mathrm{b}\cos^2\theta\\ H_\mathrm{E}\left(1+e^{-2ik_z\cdot d_z}\right) & 0 & H_\mathrm{E}+H_\mathrm{b}-H_\mathrm{a} & 0\end{pmatrix}\begin{pmatrix}\delta m_1^a\\ \delta m_1^{||}\\ \delta m_2^a\\ \delta m_2^{||}\end{pmatrix}. \tag{18}$$

We solve this to extract the dispersion relation in Fig. 3a of the main text.

In Fig. 8 we show the dependance of the modes on gyromagnetic ratio, anisotropies and interlayer exchange. They mirror those shown in Fig. 3 of the main text for the numerical model. We also see that increasing H_a and decreasing H_b has a similar effect on the frequencies, and thus we fix H_b for all fits to avoid overfitting.

5 Layer-resolved macrospin model

For the layer-resolved macrospin model, we again introduce a layer-dependent effective field into the LL equation. Now, however, the parameters can be varied independently from each other in each layer. We start with the LL equation

$$\frac{d\vec{m}_i}{dt} = -\gamma_i\vec{m}_i\times\vec{H}_{\mathrm{eff}_i} \tag{19}$$

where γ_i is the layer-dependent gyromagnetic ratio. The energy of the system is given by

$$E = -\vec{H}_0\sum_i\vec{m}_i + \sum_{\langle i,j\rangle}H_{\mathrm{E}_{ij}}\vec{m}_i\cdot\vec{m}_j - \frac{1}{2}\sum_i H_{\mathrm{a}_i}\left(m_i^\mathrm{a}\right)^2 - \frac{1}{2}H_\mathrm{b}\sum_i\left(m_i^\mathrm{b}\right)^2. \tag{20}$$

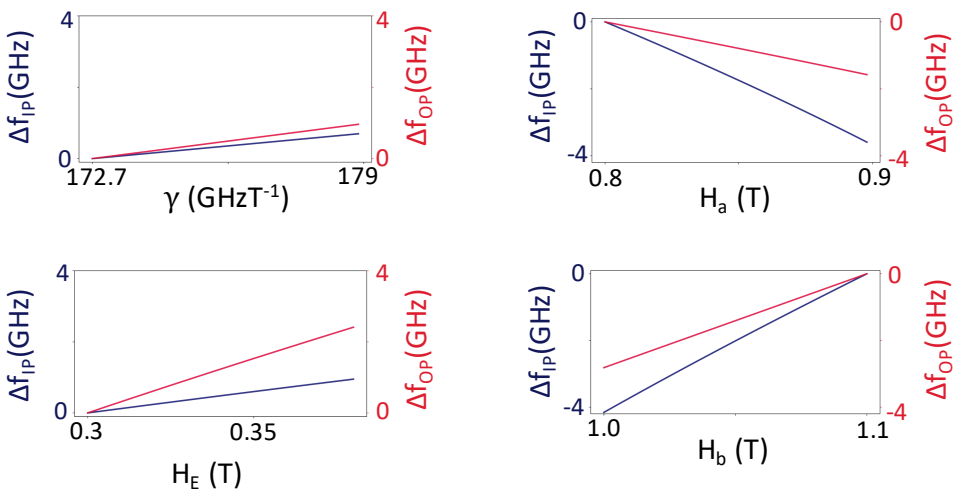

Figure 8: **Analytical macrospin model** Influence of changing (a) γ, (b) H_E, (c) H_a and (d) H_b on the magnon modes.

We now use explicitly layer-dependent parameters, in particular the interlayer exchange interaction between layers i and j, $H_{\mathrm{E}_{i,j}}$, as well as the intermediate axis anisotropy in individual layers i, H_{a_i}. The external field and easy-axis anisotropy remain layer-independent. The effective field in layer i then results to

$$\vec{H}_{\mathrm{eff}_i} = -\nabla_{\vec{m}_i} E = \vec{H}_0 - \sum_{<i,j>} H_{E_{i,j}} \vec{m}_j + H_{\mathrm{a}_i} m_i^{\mathrm{a}} \hat{a} + H_\mathrm{b} m_i^{\mathrm{b}} \hat{b}. \tag{21}$$

We can still describe the equilibrium macrospins $\vec{m}_{i,0}$ by their tilt angle θ_i away from the easy $\hat{b}$-axis: $\vec{m}_{i,0} = (0, \sin\theta_i, \pm\cos\theta_i)$. However, the θ_i are now layer-dependent. By minimizing the energy in Eq. (20) with respect to the θ_i, we can find their equilibrium position, analogous to the bulk model in Eq. (12). For three layers, the explicit system of equations is

$$\frac{\mathrm{d}E}{\mathrm{d}\theta_1} = -H_0 \cos\theta_1 + H_{\mathrm{E}_{1,2}}(\cos\theta_1 \sin\theta_2 + \sin\theta_1 \cos\theta_2) + H_\mathrm{b} \cos\theta_1 \sin\theta_1 = 0 \tag{22}$$

$$\frac{\mathrm{d}E}{\mathrm{d}\theta_2} = -H_0 \cos\theta_2 + H_{\mathrm{E}_{1,2}}(\cos\theta_2 \sin\theta_1 + \sin\theta_2 \cos\theta_1) + H_{\mathrm{E}_{2,3}}(\cos\theta_2 \sin\theta_3 + \sin\theta_2 \cos\theta_3) + H_\mathrm{b} \cos\theta_2 \sin\theta_2 = 0 \tag{23}$$

$$\frac{\mathrm{d}E}{\mathrm{d}\theta_3} = -H_0 \cos\theta_3 + H_{\mathrm{E}_{2,3}}(\cos\theta_3 \sin\theta_2 + \sin\theta_3 \cos\theta_2) + H_\mathrm{b} \cos\theta_3 \sin\theta_3 = 0, \tag{24}$$

which we solve numerically.

Next, we again linearize the LL equation in Eq. (19) and write $\delta\vec{m}_i = \left(\delta m_i^{\mathrm{a}}, \mp\delta m_i^{||} \cos\theta_i, \delta m_i^{||} \sin\theta_i\right)$. Inserting this into Eq. (13) and using the ansatz $\delta\vec{m}_i(t) = \delta\vec{m}_i(t=0)e^{-i\omega t}$ results in the following matrix equation for the case of three layers:

$$\frac{i\omega}{\gamma}\begin{pmatrix} \delta m_1^a \\ \delta m_1^{||} \\ \delta m_2^a \\ \delta m_2^{||} \\ \delta m_3^a \\ \delta m_3^{||} \end{pmatrix} = \begin{pmatrix} 0 & -H_{E_{1,2}}\frac{\cos\theta_2}{\cos\theta_1} - H_\mathrm{b}\cos^2\theta_1 & 0 & H_{E_{1,2}}\cos(\theta_1+\theta_2) & 0 & 0 \\ H_{E_{1,2}}\frac{\cos\theta_2}{\cos\theta_1} + H_\mathrm{b} - H_{a_1} & 0 & H_{E_{1,2}} & 0 & 0 & 0 \\ 0 & H_{E_{1,2}}\cos(\theta_1+\theta_2) & 0 & -H_{E_{1,2}}\frac{\cos\theta_1}{\cos\theta_2} - H_{E_{2,3}}\frac{\cos\theta_3}{\cos\theta_2} - H_\mathrm{b}\cos^2\theta_2 & 0 & H_{E_{2,3}}\cos(\theta_2+\theta_3) \\ H_{E_{1,2}} & 0 & H_{E_{1,2}}\frac{\cos\theta_1}{\cos\theta_2} + H_{E_{2,3}}\frac{\cos\theta_3}{\cos\theta_2} + H_\mathrm{b} - H_{a_2} & 0 & H_{E_{2,3}} & 0 \\ 0 & 0 & 0 & H_{E_{2,3}}\cos(\theta_2+\theta_3) & 0 & -H_{E_{2,3}}\frac{\cos\theta_2}{\cos\theta_3} - H_\mathrm{b}\cos^2\theta_3 \\ 0 & 0 & H_{E_{2,3}} & H_{E_{2,3}}\frac{\cos\theta_2}{\cos\theta_3} + H_\mathrm{b} - H_{a_3} & 0 & \end{pmatrix} \begin{pmatrix} \delta m_1^a \\ \delta m_1^{||} \\ \delta m_2^a \\ \delta m_2^{||} \\ \delta m_3^a \\ \delta m_3^{||} \end{pmatrix} \tag{25}$$

which can be solved numerically. Eq. (25) can be expanded for an arbitrary amount of layers N. For large N, we extract the k_z value of each eigenmode via Fast Fourier transform and arrive at the dispersion relation for thick samples, as shown in the main text Fig. 3a for $N = 100$.

6 Excitation of coherent magnon modes by laser pulses

In thick samples, previous studies have established that light pulses excite the optical and acoustic mode around $k_z \approx 0$ [7, 8]. In thin samples, however, the spacing along the z-direction becomes discrete, so that the notion of a wavevector k_z loses meaning. Therefore, we need to establish which modes in the layer-resolved macrospin model correspond to the modes we excite and probe in the experiment in few-layer samples (and to what modes in bulk samples they correspond). We use the following set of assumptions to estimate the coupling of the eigenmodes to excitation by light:

- The ultrafast pump pulse leads to a step-like change in the layer-resolved effective fields:

$$\vec{H}_{\mathrm{eff}_j}(t > 0) = \vec{H}_{\mathrm{eff}_j}(t < 0) + \Delta\vec{H}_{\mathrm{eff}_j} \tag{26}$$

- This step-like change can be in the same direction across layers – e.g. due to heating decreasing the exchange interaction – or alternate in direction in every second layer – e.g. due to magnetoelastic coupling [9]:

$$\Delta\vec{H}_{\mathrm{eff}_j} = \Delta\vec{H}_{\mathrm{eff}_{\mathrm{even}}} + (-1)^j \Delta\vec{H}_{\mathrm{eff}_{\mathrm{odd}}} \tag{27}$$

- The change in effective field leads to a new equilibrium macrospin position:

$$\vec{m}_{0,j}(t > 0) = \vec{m}_{0,j}(t < 0) + \Delta\vec{m}_j \tag{28}$$

- After the excitation, the macrospins want to align along their new equilibrium positions, leading to magnon oscillations. We use the projection of the eigenmodes before the laser pulse $\delta\vec{m}_j(t < 0)$ onto the $\Delta\vec{m}_j$ resulting from the aforementioned excitation as an estimate of how efficiently each eigenmode $\delta\vec{m}_j(t < 0)$ is excited by light:

$$\delta\vec{m}_j(t < 0) \cdot \Delta\vec{m}_j = \delta\vec{m}_j(t < 0) \cdot (\vec{m}_{0,j}(t > 0) - \vec{m}_{0,j}(t < 0)) \tag{29}$$

- We assume that $|m_{j,0}| = const.$, and therefore $\vec{m}_{j,0}(t < 0) \cdot \delta\vec{m}_j(t < 0) = 0$, so that the projection is simply given by

$$\delta\vec{m}_j(t < 0) \cdot \vec{m}_{0,j}(t > 0) \tag{30}$$

First, we model an excitation which is homogeneous across layers, changing the effective field by

$$\Delta\vec{H}_{\mathrm{eff}_{\mathrm{even,i}}} = -\Delta H_{\mathrm{E}_{ij}} \frac{\vec{H}_{\mathrm{E}_{ij}}}{|\vec{H}_{\mathrm{E}_{ij}}|}, \tag{31}$$

i.e. reducing the interlayer exchange in every layer. To account for heating effects, we include a gradient in $\Delta H_{\mathrm{E}_{ij}}$ (resulting layer-dependent exchange interaction after laser excitation in Fig. 9a). As a result of the decreased exchange interaction, the equilibrium macrospin position after excitation points more along the $\hat{c}$-direction in all layers:

$$\vec{m}_{i,0}(t > 0) = \vec{m}_{i,0}(t < 0) + \Delta m_i \hat{c}. \tag{32}$$

Now, we calculate the projection $\delta\vec{m}_i(t < 0) \cdot \vec{m}_{i,0}(t > 0)$ for this case, shown colorcoded in the layer-dependent eigenvalues in Fig. 9b. For large N, the projection is largest for the lowest frequency bulk modes (yellow dots at $\sim 20\,\mathrm{GHz}$), which is consistent with the f_{IP} of bulk measurements [7]. For small N, one of the edge modes starts to couple strongly to light as it spreads across the sample (light green dots with lowest f for $N < 10$), while the

coupling of the former f_{IP} becomes weaker. Therefore we assign the corresponding eigenvalue of this edge mode to the experimental f_{IP} in few-layer devices.

Next, we explore the effect of an alternating laser-pulse-induced change across layers, e.g. an additional effective field term along the c-direction due to magnetoelastic coupling [9]:

$$\Delta\vec{H}_{\mathrm{eff}_{\mathrm{odd,j}}} = (-1)^j \Delta H_{\mathrm{T}_j} \hat{c}. \tag{33}$$

As $\vec{H}_0 = H_0\hat{c}$ in our model, we introduce this additional effective field as a change in H_0, including a gradient due to heating effects (see Fig. 9c). The new equilibrium macrospin positions after excitation now alternate between layers:

$$\vec{m}_{0,j}(t > 0) = \vec{m}_{0,j}(t < 0) + (-1)^j \Delta m_j \hat{c}. \tag{34}$$

The resulting projections are shown colorcoded in Fig. 9d. The largest projection is seen for the highest frequency mode – corresponding to the f_{OP} ($k_z \approx 0$) mode in bulk experiments. For small N, the largest projection also belongs to the mode with the largest eigenvalue, which we therefore assign to our experimental f_{OP} (at $N = 3$ the bulk f_{IP} and f_{OP} modes converge). In Fig. 3b of the main text, the modes are colored according to the coupling to a homogeneous (blue) vs. alternating (red) excitation.

In Fig. 9e, f we show the components m_a and $m_{||}$ for the trilayer modes. The mode f_{middle} (bright blue) is asymmetric across the device, while f_{IP} (dark blue) and f_{OP} (red) are symmetric. An excitation by light should have a similar effect in every second layer (due to the long wavelength of light compared to the sample thickness), and therefore cannot couple to the f_{middle} mode. In Fig. 9g, h we show the f_{IP} (dark blue) and f_{OP} (red) and the two edge modes (bright blue, green) in a 100-layer device. The edges modes are confined to the first ~ 8 layers. The f_{IP} and f_{OP} modes spread across the complete bulk and have the maximum possible real space wavelength, i.e. minimal k_z, which is consistent with the argumentation in previous studies that light excitation couples to these two modes.

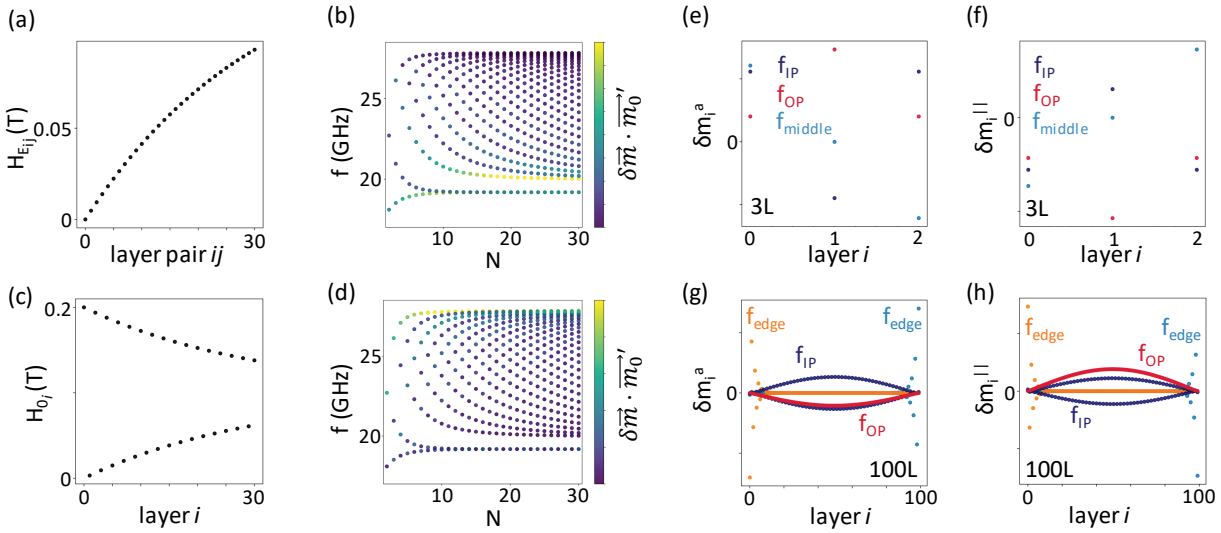

Figure 9: **Numerical macrospin model** (a) Homogeneous change in H_E across layers (e.g. due to heating) leads to (b) a strong coupling with the acoustic mode for bulk samples or the "surface" mode for thin samples. (c) An alternating change in H_0 (which is expected to arise from, e.g., magnetoelastic effects) strongly couples to excitation of the optical mode (d). (e-f) Mode shapes of the trilayer. (g-h) Surface modes and example of a bulk mode for a 100-layer device.

7 Macrospin fit results

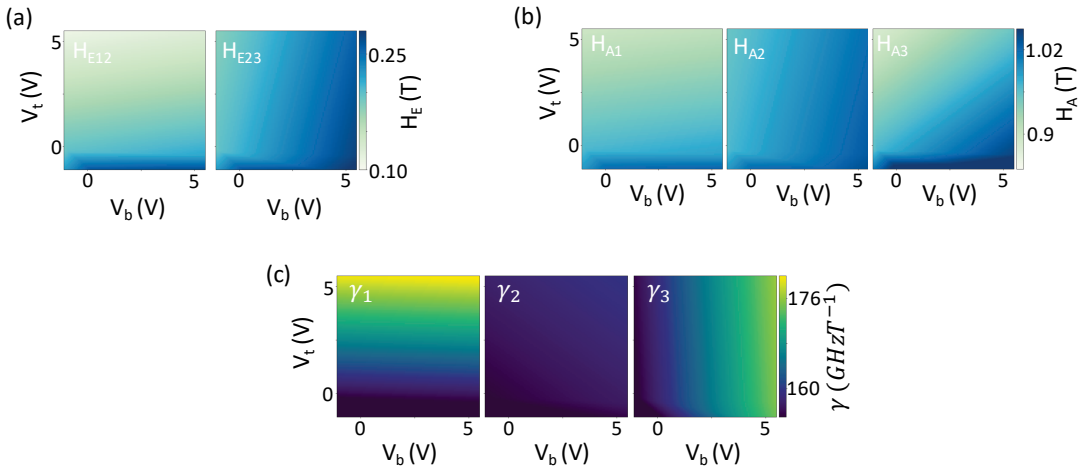

Figure 10: **Macrospin fitting results trilayer** The results of the macrospin model fitted to the capacitor model for the (a) exchange fields, (b) anisotropy fields and (c) gyromagnetic ratios.

Using the dependencies from the main text and the results from Fig. 5, we fit the lowest and highest eigenvalue of Eq. (25) to the observed gate-dependent f_{IP} and f_{OP} of the trilayer. We use the resulting fitting parameters from Table 1 of the main text to calculate the interlayer exchange and intermediate axis anisotropy fields and gyromagnetic ratios for each layer in Fig. 10.

The maximum changes in gyromagnetic ratio we predict in the top layer roughly correspond to a change of 2.75 to 3.2 μ_B per Cr atom, which is an order of magnitude more than predicted for CrSeBr by doping [10]. Our dependence of anisotropy on electric field of $-0.8\,\mathrm{T\,nm\,V^{-1}}$ corresponds to $\sim -600\,\mathrm{fJ\,V^{-1}\,m^{-1}}$ of changes in anisotropy constant per unit surface per unit electric field. For comparison, usual voltage controlled magnetic anisotropy (VCMA) coefficients describing changes of interfacial perpendicular magnetic aniostropy at ferromagnet-oxide interfaces reach around $\sim -100\,\mathrm{fJ\,V^{-1}\,m^{-1}}$ [11–13]. The tunability we reach in the interlayer exchange field is comparable to that in bulk CrSBr when applying in-plane strain [14], however, the exchange interaction becomes stronger rather than weaker.

We do the same calculations for the 5- and 8-layer devices using the results of the electrostatic modelin in Figs. 6 and 7 and the fitting parameters from Table 1 of the main text. The resulting internal fields and gyromagnetic ratios are shown in Figs. 11 and 12.

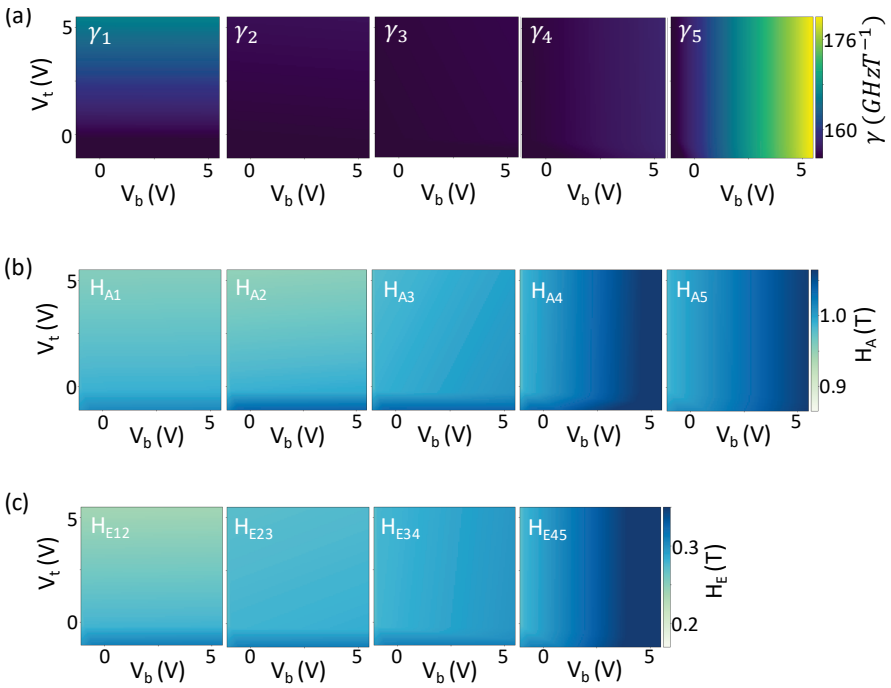

Figure 11: **Macrospin fitting results 5-layer** The results of the macrospin model fitted to the capacitor model for the (a) gyromagnetic ratios, (b) anisotropy fields and (c) interlayer exchange fields.

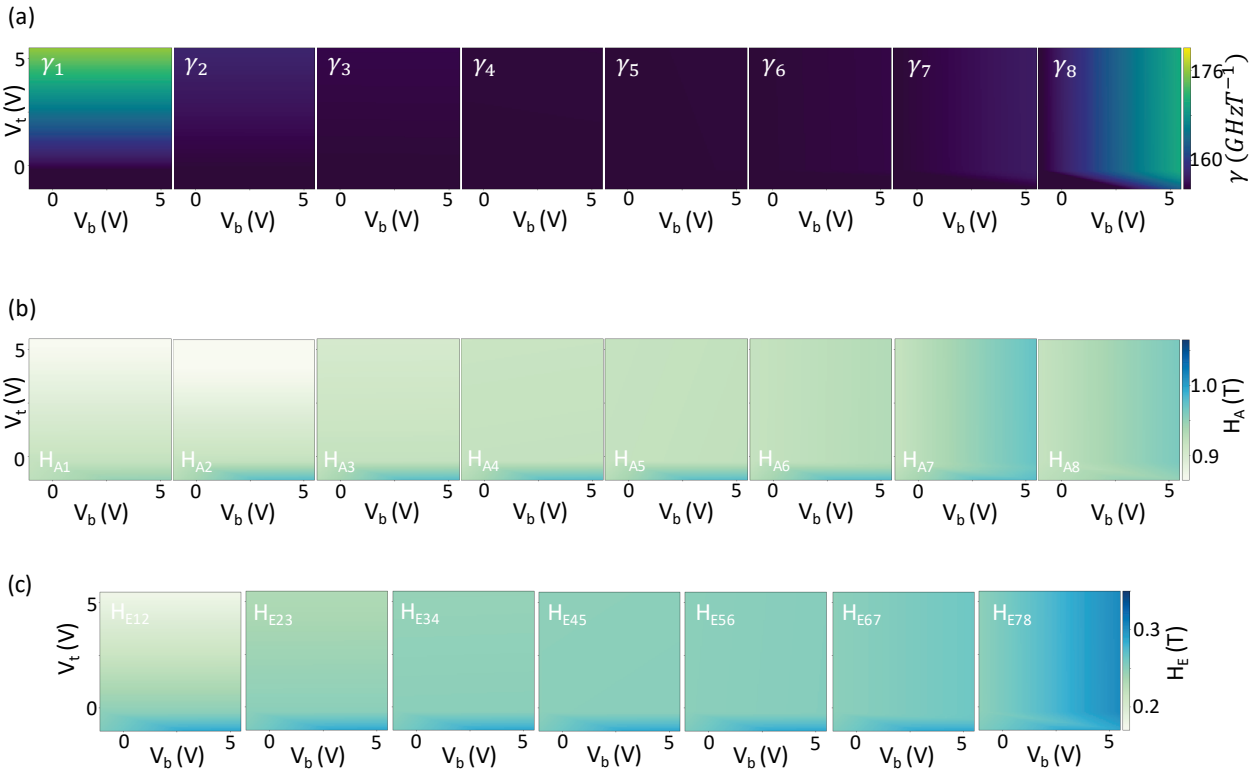

Figure 12: **Macrospin fitting results 8-layer** The results of the macrospin model fitted to the capacitor model for the (a) gyromagnetic ratios, (b) anisotropy fields and (c) interlayer exchange fields.

8 Gate dependence of magnons in 8-layer device

The compelete gate-dependence of the magnons in 8 layers is shown in Fig. 13 together with the macrospin modeling. Overall, the model predicts the experimentally observed frequecies. There are discrepancies mainly in the doping dependence of f_{IP} (top left panel). These could be due to some simplifications we made for fitting: For example, we fixed $H_b = 1.3\,\mathrm{T}$ in all devices. However, H_b could vary slightly between edgexfoliated flakes – this can lead to differences in ν_{a} across samples. This could result in over- or underestimating changes in f_{IP} for certain field- and doping conditions. This is reflected in the larger errors for the 8-layer fitting results in Table 1 of the main text.

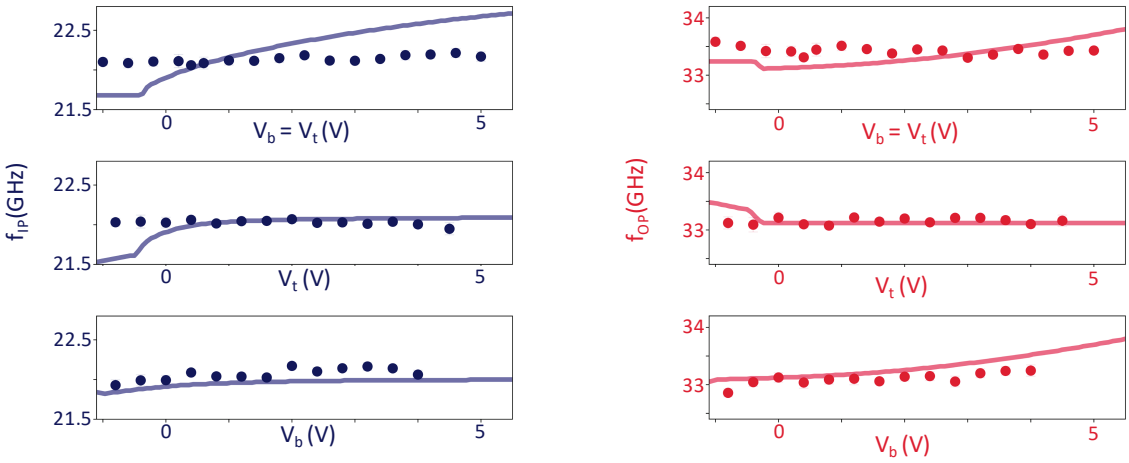

Figure 13: **Gate-dependent magnon frequencies of 8-layer device** Complete gate-dependence of (a) f_{IP} and (b) f_{OP} in the 8-layer device (dots: experimental data, solid lines: macrospin model).

9 Gate-dependent magnetic phenomena

As mentioned in the main text, multiple gating effects on magnetic properties have been suggested as illustrated in Fig. 14. (1) By increasing the electron doping n, the magnitude of the gyromagnetic ratio γ of the macrospins can increase due to an increase in carriers with magnetic moment [10]. The Coulomb repulsion parameter U can increase with n, possibly influencing the exchange constants according to the Kugel-Khomskii model [15–17]. (2) When doping with electrons, e_g levels will be populated in addition to t_{2g} ones [16–18]. This can change the orbitals involved in the hopping between sites, again affecting the (anti-)ferromagnetic exchange coupling parameters. Additionally, the different orbital shapes can influence the anisotropy of the material [19]. (3) A perpendicular electric field between layers can shift the energy positons of bands associated with different orbitals in neighboring layers with respect to each other, again influencing the (anti-)ferromagnetic exchange coupling parameter [20]. (4) Gates can influence orbital filling especially in the outer layers due to the resulting electric field, as electrons want to reside further/closer to the gate, shuffling them into $d_{x^2-y^2}$ or d_{z^2} orbitals, respectively. This is commonly called voltage-induced magnetic anisotropy [11, 21, 22].

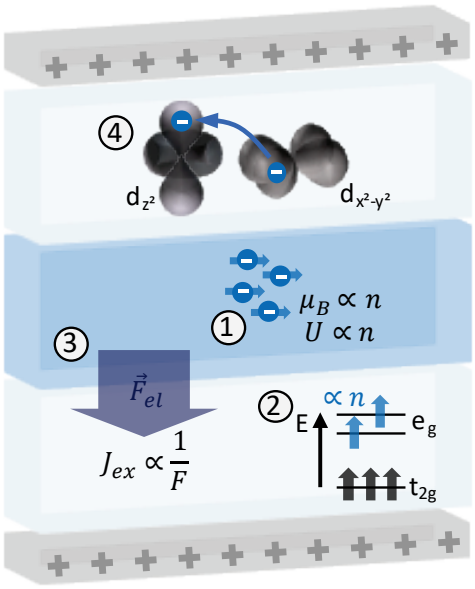

Figure 14: **Possible doping- and field related effects on magnetic parameters** Sketch of possible gating effects on gyromagnetic ratio, anisotropy and exchange fields.

10 Thickness measurement of CrSBr flakes

To find the layer number of the measured flakes, we performed AFM measurements (Fig. 15). We find the following thicknesses – Sample 1: 2.4 nm, Sample 2: 4 nm, Sample 1: 6.4 nm – corresponding to 3, 5 and 8 layers, respectively [23].

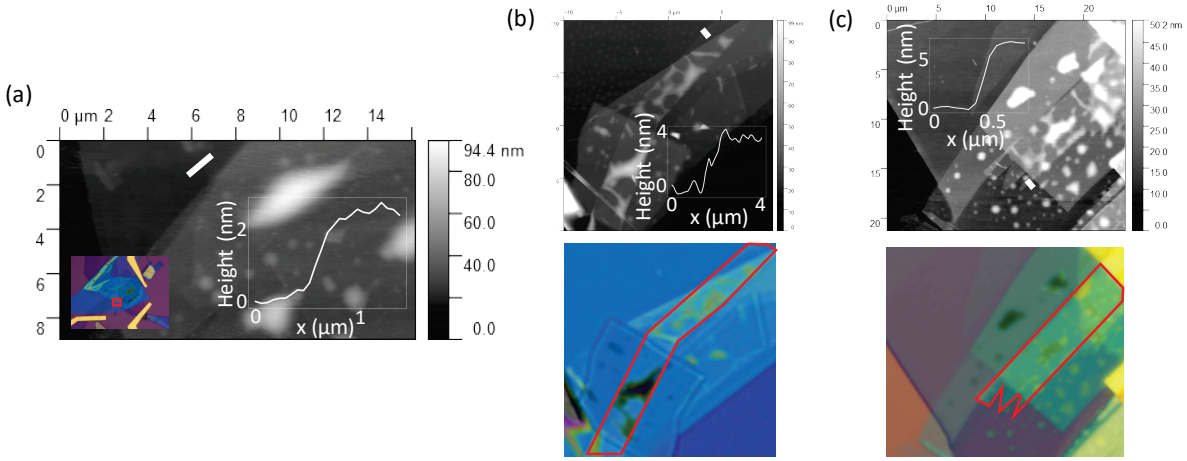

Figure 15: **AFM images** (a) AFM image of a small portion of the trilayer device (marked in optical image). The height profile corresponds to a linecut of the CrSBr flake along the marker in the image. (b) AFM (top) and corresponding optical (bottom, CrSBr flake outlined) image of the 5-layer device before contact patterning. The height profile corresponds to a linecut of the CrSBr flake along the marker in the image. (c) AFM (top) and corresponding optical (bottom, CrSBr flake outlined) image of the 8-layer device before contact patterning. The height profile corresponds to a linecut of the CrSBr flake along the marker in the image.

References

[1] David C. Meeker. Finite Element Method Magnetics, version 4.2 (https://www.femm.info).

[2] Riccardo Pisoni, Tim Davatz, Kenji Watanabe, Takashi Taniguchi, Thomas Ihn, and Klaus Ensslin. Absence of interlayer tunnel coupling of K-valley electrons in bilayer MoS_2. *Physical Review Letters*, 123:117702, 9 2019.

[3] Sviatoslav Kovalchuk, Kyrylo Greben, Abhijeet Kumar, Simon Pessel, Kenji Watanabe, Takashi Taniguchi, Dominik Christiansen, Malte Selig, Andreas Knorr, and Kirill I. Bolotin. Interlayer excitons in semiconductor bilayers under a strong electric field. arxiv.org/abs/2303.09931v1, 2023.

[4] Akash Laturia, Maarten L. Van de Put, and William G. Vandenberghe. Dielectric properties of hexagonal boron nitride and transition metal dichalcogenides: from monolayer to bulk. *npj 2D Materials and Applications 2018 2:1*, 2:1–7, 3 2018.

[5] Julian Klein, Benjamin Pingault, Matthias Florian, Marie Christin Heißenbüttel, Alexander Steinhoff, Zhigang Song, Kierstin Torres, Florian Dirnberger, Jonathan B. Curtis, Mads Weile, Aubrey Penn, Thorsten Deilmann, Rami Dana, Rezlind Bushati, Jiamin Quan, Jan Luxa, Zdeněk Sofer, Andrea Alù, Vinod M. Menon, Ursula Wurstbauer, Michael Rohlfing, Prineha Narang, Marko Lončar, and Frances M. Ross. The bulk van der Waals layered magnet CrSBr is a quasi-1D material. *ACS Nano*, 17:5316–5328, 3 2023.

[6] Florian Dirnberger, Rezlind Bushati, Biswajit Datta, Ajesh Kumar, Allan H. MacDonald, Edoardo Baldini, and Vinod M. Menon. Spin-correlated exciton–polaritons in a van der Waals magnet. *Nature Nanotechnology 2022 17:10*, 17:1060–1064, 9 2022.

[7] Youn Jue Bae, Jue Wang, Allen Scheie, Junwen Xu, Daniel G. Chica, Geoffrey M. Diederich, John Cenker, Michael E. Ziebel, Yusong Bai, Haowen Ren, Cory R. Dean, Milan Delor, Xiaodong Xu, Xavier Roy, Andrew D. Kent, and Xiaoyang Zhu. Exciton-coupled coherent magnons in a 2D semiconductor. *Nature 2022 609:7926*, 609:282–286, 9 2022.

[8] Yue Sun, Fanhao Meng, Changmin Lee, Aljoscha Soll, Hongrui Zhang, Ramamoorthy Ramesh, Jie Yao, Zdeněk Sofer, and Joseph Orenstein. Dipolar spin wave packet transport in a van der Waals antiferromagnet. *Nature Physics 2024*, pages 1–7, 2 2024.

[9] Youn Jue Bae, Taketo Handa, Yanan Dai, Jue Wang, Huicong Liu, Allen Scheie, Daniel G. Chica, Michael E. Ziebel, Andrew D. Kent, Xiaodong Xu, Ka Shen, Xavier Roy, and Xiaoyang Zhu. Transient magnetoelastic coupling in CrSBr. *Physical Review B*, 109:104401, 1 2024.

[10] Ruilin Han, Xiaomin Xue, and Peng Li. Enhanced ferromagnetism, perpendicular magnetic anisotropy and high Curie temperature in the van der Waals semiconductor CrSeBr through strain and doping. *Physical Chemistry Chemical Physics*, 26:12219–12230, 4 2024.

[11] Bivas Rana, Samiran Choudhury, Katsuya Miura, Hiromasa Takahashi, Anjan Barman, and Yoshi Chika Otani. Electric field control of spin waves in ultrathin CoFeB films. *Physical Review B*, 100:224412, 12 2019.

[12] Xiang Li, Kevin Fitzell, Di Wu, C. Ty Karaba, Abraham Buditama, Guoqiang Yu, Kin L. Wong, Nicholas Altieri, Cecile Grezes, Nicholas Kioussis, Sarah Tolbert, Zongzhi Zhang, Jane P. Chang, Pedram Khalili Amiri, and

Kang L. Wang. Enhancement of voltage-controlled magnetic anisotropy through precise control of Mg insertion thickness at CoFeB|MgO interface. *Applied Physics Letters*, 110:52401, 1 2017.

[13] Takayuki Nozaki, Kay Yakushiji, Shingo Tamaru, Masaki Sekine, Rie Matsumoto, Makoto Konoto, Hitoshi Kubota, Akio Fukushima, and Shinji Yuasa. Voltage-induced magnetic anisotropy changes in an ultrathin FeB layer sandwiched between two MgO layers. *Applied Physics Express*, 6:073005, 7 2013.

[14] Geoffrey M. Diederich, John Cenker, Yafei Ren, Jordan Fonseca, Daniel G. Chica, Youn Jue Bae, Xiaoyang Zhu, Xavier Roy, Ting Cao, Di Xiao, and Xiaodong Xu. Tunable interaction between excitons and hybridized magnons in a layered semiconductor. *Nature Nanotechnology 2022 18:1*, 18:23–28, 12 2022.

[15] Farsane Tabataba-Vakili, Huy P. G. Nguyen, Anna Rupp, Kseniia Mosina, Anastasios Papavasileiou, Kenji Watanabe, Takashi Taniguchi, Patrick Maletinsky, Mikhail M. Glazov, Zdenek Sofer, Anvar S. Baimuratov, and Alexander Högele. Doping-control of excitons and magnetism in few-layer CrSBr. *Nature Communications*, 12 2023.

[16] K. I. Kugel and D. I. Khomskii. Crystal structure and magnetic properties of substances with orbital degeneracy. *Zh. Eksp. Teor. Fiz.*, 64:1429–1439, 1973.

[17] K. I. Kugel and D. I. Khomskii. The Jahn-Teller effect and magnetism: Transition metal compounds. *Soviet Physics - Uspekhi*, 25:621–641, 4 1982.

[18] V. V. Mazurenko, F. Mila, and V. I. Anisimov. Electronic structure and exchange interactions of $Na_2V_3O_7$. *Physical Review B - Condensed Matter and Materials Physics*, 73:014418, 1 2006.

[19] Michael E. Ziebel, Margalit L. Feuer, Jordan Cox, Xiaoyang Zhu, Cory R. Dean, and Xavier Roy. CrSBr: An air-stable, two-dimensional magnetic semiconductor. *Nano Letters*, 24:4319–4329, 4 2024.

[20] Youwen Wang, Nannan Luo, Jiang Zeng, Li Ming Tang, and Ke Qiu Chen. Magnetic anisotropy and electric field induced magnetic phase transition in the van der Waals antiferromagnet CrSBr. *Physical Review B*, 108:054401, 8 2023.

[21] T. Maruyama, Y. Shiota, T. Nozaki, K. Ohta, N. Toda, M. Mizuguchi, A. A. Tulapurkar, T. Shinjo, M. Shiraishi, S. Mizukami, Y. Ando, and Y. Suzuki. Large voltage-induced magnetic anisotropy change in a few atomic layers of iron. *Nature Nanotechnology 2009 4:3*, 4:158–161, 1 2009.

[22] K. H. He, J. S. Chen, and Y. P. Feng. First principles study of the electric field effect on magnetization and magnetic anisotropy of FeCo/MgO(001) thin film. *Applied Physics Letters*, 99:72503, 8 2011.

[23] Evan J. Telford, Avalon H. Dismukes, Raymond L. Dudley, Ren A. Wiscons, Kihong Lee, Daniel G. Chica, Michael E. Ziebel, Myung Geun Han, Jessica Yu, Sara Shabani, Allen Scheie, Kenji Watanabe, Takashi Taniguchi, Di Xiao, Yimei Zhu, Abhay N. Pasupathy, Colin Nuckolls, Xiaoyang Zhu, Cory R. Dean, and Xavier Roy. Coupling between magnetic order and charge transport in a two-dimensional magnetic semiconductor. *Nature Materials 2022 21:7*, 21:754–760, 5 2022.